bioRxiv preprint doi: https://doi.org/10.1101/2020.07.04.187989; this version posted July 4, 2020. The copyright holder for this preprint (which was not certified by peer review) is the author/funder. This article is a US Government work. It is not subject to copyright under 17 USC 105 and is also made available for use under a CC0 license.

A pH-dependent switch mediates conformational masking of SARS-CoV-2 spike

Tongqing Zhou[1,*], Yaroslav Tsybovsky[2,*], Adam S. Olia[1,*], Jason Gorman[1], Micah A. Rapp[3], Gabriele Cerutti[3], Phinikoula S. Katsamba[3], Alexandra Nazzari[1], Arne Schön[4], Pengfei Wang[5], Jude Bimela[3], Wei Shi[1], I-Ting Teng[1], Baoshan Zhang[1], Jeffrey C. Boyington[1], Gwo-Yu Chuang[1], Jared M. Sampson[3,6], Mallika Sastry[1], Tyler Stephens[2], Jonathan Stuckey[1], Shuishu Wang[1], Richard A. Friesner[6], David D. Ho[5], John R. Mascola[1], Lawrence Shapiro[1,3,5], Peter D. Kwong[1,3]

[1] Vaccine Research Center, National Institute of Allergy and Infectious Diseases, National Institutes of Health, Bethesda, MD 20892, USA.
[2] Electron Microscopy Laboratory, Cancer Research Technology Program, Leidos Biomedical Research, Inc., Frederick National Laboratory for Cancer Research, Frederick, MD 21702, USA.
[3] Department of Biochemistry and Molecular Biophysics, Columbia University, New York, NY 10032, USA.
[4] Department of Biology, Johns Hopkins University, Baltimore, MD, 21218, USA.
[5] Aaron Diamond AIDS Research Center, Columbia University Vagelos College of Physicians and Surgeons, New York, NY 10032, USA.
[6] Department of Chemistry, Columbia University, New York, NY 10027, USA.

[*] These authors contributed equally to this work.

bioRxiv preprint doi: https://doi.org/10.1101/2020.07.04.187989; this version posted July 4, 2020. The copyright holder for this preprint (which was not certified by peer review) is the author/funder. This article is a US Government work. It is not subject to copyright under 17 USC 105 and is also made available for use under a CC0 license.

SARS-CoV-2 has emerged as a global pathogen[1,2], sparking urgent vaccine development efforts with the trimeric spike[3,4]. However, the inability of antibodies like CR3022[5], which binds a cryptic spike epitope with nanomolar affinity[6], to neutralize virus, suggests a spike-based means of neutralization escape. Here, we show the SARS-CoV-2 spike to have 10% the unfolding enthalpy of a globular protein at physiological pH, where it is recognized by antibodies like CR3022, and up to 10-times more unfolding enthalpy at endosomal pH, where it sheds such antibodies, suggesting that the spike evades potentially neutralizing antibody through a pH-dependent mechanism of conformational masking. To understand the compatibility of this mechanism with ACE2-receptor interactions, we carried out binding measurements and determined cryo-EM structures of the spike recognizing up to three ACE2 molecules at both physiological and endosomal pH. In the absence of ACE2, cryo-EM analyses indicated lower pH to reduce conformational heterogeneity. Single-receptor binding domain (RBD)-up conformations dominated at pH 5.5, resolving into a locked all-down conformation at lower pH through lowering of RBD and refolding of a pH-dependent switch. Notably, the emerging Asp614Gly strain[7] partially destabilizes the switch that locks RBD down, thereby enhancing functional interactions with ACE2 while reducing evasion by conformational masking.

The SARS-CoV-2 spike is a type 1 fusion machine, responsible for virus-cell entry via ACE2 receptor interactions and TMPRSS2 protease activation in the endosome[8]. It is substantially glycosylated[9,10]. It is also divergent from other beta-coronavirus pathogens known to have infected humans[2], and it continues to diversify[7]. Cryo-EM structures of the SARS-CoV-2 spike[3,4] reveal two prevalent conformations: a single-up conformation and an all-down conformation, related to

bioRxiv preprint doi: https://doi.org/10.1101/2020.07.04.187989; this version posted July 4, 2020. The copyright holder for this preprint (which was not certified by peer review) is the author/funder. This article is a US Government work. It is not subject to copyright under 17 USC 105 and is also made available for use under a CC0 license.

the orientations of the receptor-binding domains (RBDs). However, the extent to which spike glycosylation, sequence diversity, and conformational heterogeneity impact antibody elicitation or antibody-mediated neutralization is unclear.

Accumulating data indicates that individuals who recover from COVID-19 often do not have high levels of neutralizing antibody activity[11], and there are worrisome reports of re-infection of recovered individuals[12-14]. Moreover, reports of antibody CR3022 disassembling spike[15] suggest unusual fragility.

To facilitate a molecular understanding of the SARS-CoV-2 spike and its evasion from antibody, we measured the unfolding enthalpy of the spike as well as its binding to CR3022 antibody and to ACE2 receptor as a function of pH. We also determined cryo-EM structures of the spike, alone and in complex with ACE2 receptor, at physiological and endosomal pHs. We delineated the molecular mechanism that mediates the raising and closing of RBDs, which utilizes a refolding region with multiple aspartic acid residues, a pH-dependent switch, which when fully protonated locks RBDs in the down position. Overall, our findings suggest a pH-dependent mechanism of conformational masking, whereby reduced folding at physiological pH underlies the ease by which antibodies like CR3022 bind to spike and their prevalent elicitation. Recognition of ACE2, however, leads to endosomal entry, resulting in reduction of pH and induction of antibody shedding through pH-dependent conformational changes of the spike.

Spike at physiological pH is at a minimum of unfolding enthalpy

To provide insight into the stability of the spike over the course of virus-cell entry, we used differential scanning calorimetry (DSC) to measure the unfolding enthalpy of the soluble trimeric ectodomain (spike), which included GSAS and PP mutations and the T4 phage fibritin

bioRxiv preprint doi: https://doi.org/10.1101/2020.07.04.187989; this version posted July 4, 2020. The copyright holder for this preprint (which was not certified by peer review) is the author/funder. This article is a US Government work. It is not subject to copyright under 17 USC 105 and is also made available for use under a CC0 license.

trimerization domain[4,16], as a function of pH. Notably, at physiological pH we observed spike to be at a minimum of unfolding enthalpy (73.3 kcal/mol) or ~10% the normalized unfolding enthalpy of the average globular protein[17] (**Fig. 1a, left**). The amount of folding energy increased rapidly as pH dropped, increasing ~10-fold by pH 6 before decreasing as pH reduced further. Analysis of melting curves (**Fig. 1a, right**) indicated three distinct peaks: a peak at ~48°C, which dominated under basic conditions and decreased at acidic conditions; a peak at ~65°C, which was barely present at physiological pH, but rapidly increased to dominate as pH dropped to 5.5-6.0; and a peak at ~55°C, which first appeared as a shoulder at pH 6, but then increased to dominate and shifted to lower temperature at pH lower than 5.5.

In sharp contrast to spike, analysis of the spike N-terminal domain (NTD) and RBD as separate proteins indicated each of them to have typical unfolding enthalpies (>90% that of the average normalized globular protein) (**Extended Data Fig. 1**).

To understand how the reduced folding enthalpy might influence spike structure, we used negative stain-electron microscopy (EM) to visualize the spike as a function of pH (**Extended Data Fig. 2**). At pH 7.4, we observed the spike to be mostly disordered. However, when pH decreased, we observed well-formed trimers, which showed some clustering at pH 5.5-6.0 before resolving into separate particles at pH 4.0-4.5. Overall, we observed concordance between the presence of well-formed trimers and folding enthalpy measured by DSC, with mostly unfolded trimers at physiological pH and substantially increased folding at endosomal pH.

Binding of ACE2 receptor and CR3022 antibody at physiological and endosomal pH

For variation in pH over the course of virus entry to impact the binding of antibody, the antibody would need to allow spike recognition of the ACE2 receptor, thereby enabling the virus

bioRxiv preprint doi: https://doi.org/10.1101/2020.07.04.187989; this version posted July 4, 2020. The copyright holder for this preprint (which was not certified by peer review) is the author/funder. This article is a US Government work. It is not subject to copyright under 17 USC 105 and is also made available for use under a CC0 license.

to enter the endosome[8]. We used isothermal titration calorimetry (ITC) to determine whether binding of CR3022 to spike was compatible with ACE2 interaction. We chose to use a monomeric version of ACE2 to test more sensitively the impact of antibody inhibition. First, we titrated ACE2 into soluble spike, and observed 1.9 ACE2 molecules to bind per spike trimer, with an affinity of 94 nM (**Fig. 1b, left**). Next, we fully titrated the antigen-binding fragment (Fab) of CR3022 into soluble spike (**Extended Data Fig. 3a**) and further titrated ACE2 into the spike-CR3022 complex formed to observe 2.3 ACE2 molecules to bind each spike-CR3022 complex, with an affinity of 130 nM (**Fig. 1b, right**). The SARS-CoV-2 spike thus appears capable of recognizing ACE2 even in the presence of antibody CR3022, indicating that CR3022-bound spikes could enter the endosomal compartment.

To gain insight into the impact of pH on ACE2 and CR3022 interactions with spike, we characterized their affinities both to spike and to RBD, expressed as a separate molecule, at physiological and endosomal pH. We chose to use dimeric ACE2 to more closely mimic native interactions with spike. At endosomal pHs, surface plasmon resonance (SPR)-determined ACE2 binding affinities to both spike and RBD were somewhat reduced from 0.82 nM to 7.0 nM and from 1.0 nM to 14 nM at pH 4.5 for spike and RBD, respectively (**Extended Data Fig. 3b**). With CR3022 IgG, affinities were high to both spike and RBD at physiological pH, though with a 10-fold difference (0.49 and 0.052 nM to spike and RBD, respectively) (**Fig. 1c**). At pH 5.5, this 10-fold difference in affinity was retained (1.7 and 0.23 nM, respectively). However, at pH 4.5, CR3022 still bound to RBD (1.1 nM), but affinity to spike was dramatically reduced with a K_D > 1000 nM – an affinity difference of at least ~1000-fold (**Fig. 1c, Extended Data Fig. 3c**). Because CR3022 still bound strongly to the isolated RBD, we attribute the dramatically reduced affinity of CR3022 for spike at low pH to conformational constraints of the spike (**Fig. 1d**).

bioRxiv preprint doi: https://doi.org/10.1101/2020.07.04.187989; this version posted July 4, 2020. The copyright holder for this preprint (which was not certified by peer review) is the author/funder. This article is a US Government work. It is not subject to copyright under 17 USC 105 and is also made available for use under a CC0 license.

Cryo-EM structures of SARS-CoV-2 spike with ACE2 at physiological and endosomal pH

Structures of ACE2 and CR3022 have been determined in complex with RBD as a separate domain[6,18-20], but less is known about their interactions with trimer. To provide structural insight into the recognition between ACE2 and spike trimer, we mixed soluble ACE2 with spike trimer at a 6:1 molar ratio at pH 7.4 and collected single-particle cryo-EM data on a Titan Krios. We observed spike binding ACE2 at stoichiometries of 1:1, 1:2, and 1:3 with prevalences of 15%, 43%, and 38%, respectively (**Fig. 2a**). While the membrane-proximal region of the spike in these complexes remained 3-fold symmetric, the ACE2-binding regions showed asymmetry with, for example, superposition of the double-ACE2-bound complex onto itself based on membrane-proximal regions leading to displacement of ACE2 molecules by almost 13 Å (**Fig. 2b**). However, we could see no evidence of coordinated movement, with the RBD domain on each protomer appearing to engage ACE2 without significantly impacting the up (or down) motion of the neighboring protomers. Thus, ACE2 receptor engagement required RBD movement that did not appear to destabilize the spike nor to trigger a substantial structural rearrangement beyond raising of the RBD.

To provide insight into the impact of endosomal pH, we again mixed soluble ACE2 with spike trimer at a 6:1 molar ratio, but this time at pH 5.5, and determined the structure of the complex using cryo-EM. Similar to physiological pH, we observed spike binding ACE2 at stoichiometries of 1:1, 1:2, and 1:3 with prevalences of 27%, 32%, and 27%, respectively (**Fig. 2c**). We superposed triple-ACE2-bound complexes determined at pH 7.4 and pH 5.5 and observed the membrane-proximal regions of the spike to align closely, while ACE2 molecules showed displacements of 3.1, 6.0, and 10.8 Å (**Fig. 2d**). Overall, structures of the spike with ACE2 showed

bioRxiv preprint doi: https://doi.org/10.1101/2020.07.04.187989; this version posted July 4, 2020. The copyright holder for this preprint (which was not certified by peer review) is the author/funder. This article is a US Government work. It is not subject to copyright under 17 USC 105 and is also made available for use under a CC0 license.

about equal distribution of single-, double-, and triple-ACE2-bound states at both physiological and endosomal pH.

Ligand-free cryo-EM structures of SARS-CoV-2 spike at low pH

In light of the similarity of ACE2 complexes at pH 7.4 and 5.5 (**Fig. 2**) but substantial differences at these pHs observed for ligand-free spike by negative stain EM (**Extended Data Fig. 2**), we analyzed the structure of the spike at pH 5.5 by single-particle cryo-EM. We determined a consensus structure from 1,083,554 particles at a resolution of 2.7 Å, in which most of the spike was well resolved, except for a lone RBD for which reconstruction density was poor (**Fig. 3a; Extended Data Fig. 5a-e**). Analysis of structural heterogeneity in this region (**Supplementary Videos 1-4**; **Extended Data Fig. 5c, panel A**) produced six 3D classes ranging in prevalence from 7% to 26% and describing three principal conformations, with the RBD in the up or down position, or without a defined position for this domain (**Extended Data Fig. 5c, panel B**). Interestingly, unlike for ACE2-bound complexes, no double- or triple-RBD-up conformations were observed. Two classes with prevalences of 23% (Conformation 1 – 2.9 Å resolution) and 26% (Conformation 2 – 2.9 Å resolution) corresponded to two different single RBD-up conformations. A third prevalent class representing 10% of the particles had all RBDs down. For all three of these prevalent classes – and unlike in the consensus structure – density for all RBD domains was well resolved (**Extended Data Fig. 5c, panel C**), indicating multiple different orientations of RBD in the spike at pH 5.5. In the remaining classes, the RBD did not assume a defined position, suggesting mobility of this domain even at endosomal pH.

To determine how even lower pH affected conformational heterogeneity, and since CR3022 retained binding to spike at pH 5.5, we sought to obtain a cryo-EM structure of the ligand-

bioRxiv preprint doi: https://doi.org/10.1101/2020.07.04.187989; this version posted July 4, 2020. The copyright holder for this preprint (which was not certified by peer review) is the author/funder. This article is a US Government work. It is not subject to copyright under 17 USC 105 and is also made available for use under a CC0 license.

free spike at pH 4.0. Single particle analysis of a dataset comprising 911,839 particles resolved an all-RBD-down conformation (**Fig 3b, Extended Data Fig. 6a-b**). The map was refined to 2.4 Å resolution, enabling individual water molecules to be observed (**Fig. 3c**) and 89 additional residues to be modeled, which were undefined in published cryo-EM structures[3,4].

Refolding at spike domain interfaces underlies conformational rearrangement

To identify critical components responsible for the reduction of conformational heterogeneity between pH 5.5 and pH 4.0 – and to shed light on the mechanism locking RBDs in the down position – we analyzed root-mean square deviations (rmsds) between the pH 5.5 structures and the all-down pH 4.0 conformation with an 11-residue sliding window to identify regions that refold (**Fig. 4a (top) and Extended Data Fig. 7**). As each of the protomers in the trimer displayed a different conformation in each of the pH 5.5 structures, we defined protomer B as the one with RBD in the 'up' position in each of the single RBD-up conformations, with protomers A-C appearing counter-clockwise when viewed along the trimer 3-fold axis toward the membrane. We observed significant rmsd peaks for short stretches around residue 330 in protomers A and B, and around residue 525 in protomer B only, and most substantially in a region comprising residues 825-858 (**Extended Data Fig. 7b**). This region, which for reasons described below we named the 'switch' region, was fully defined in protomer B and partially resolved in protomer A (residues 825-829 and 849-858) and protomer C (residues 825-840 and 851-858). Notably, this region was almost entirely unresolved in our structures with ACE2 and in published spike structures[3,4] (**Fig. 4a, bottom**).

The asymmetry in distribution of refolding regions in the trimer between single-up and all-down structures (**Fig. 4b**) suggested the 'up' RBD to require concerted adjustments throughout the trimer. To delineate these, we determined angles and rigid-body translations between each of the

bioRxiv preprint doi: https://doi.org/10.1101/2020.07.04.187989; this version posted July 4, 2020. The copyright holder for this preprint (which was not certified by peer review) is the author/funder. This article is a US Government work. It is not subject to copyright under 17 USC 105 and is also made available for use under a CC0 license.

subdomains (**Extended Data Fig. 8**) for pH 5.5 single RBD-up and 4.0 all RBD-down structures. For clarity, we specify by subscript the protomer of each subunit or of each residue. Starting with the $SD1_A$ -entrance loop of protomer A, and moving laterally around the trimer (**Fig. 4c, Supplementary Video 5**), we observed slight refolding in the $313\text{-}325_A$ stretch, allowing a 17° rotation of the $SD1_A$ domain to accommodate the switch region on the neighboring B protomer (switch B). At pH 5.5, switch B interacted with $SD2_A$ (buried surface area of 296.8 $Å^2$), and this key inter-protomer contact coupled with $SD1_A$ rotation and 2.8-Å translation resulted in the 8.8-Å lateral displacement of NTD_B towards the next RBD-switch. The displaced NTD_B induced consecutive shifts of $SD2_B$ and $SD1_B$ domains, which culminated in the 22.8-Å 'up' translation (64.9° rotation) of RBD_B versus its down-equivalent.

The 'up' positioning of RBD_B was accommodated in part by a 5.1 Å mostly downwards displacement of NTD_C towards the viral membrane, which – continuing to the next RBD-switch – induced minor shifts of $SD2_C$ and $SD1_C$ domains and yielded RBD_C and switch A in conformations that closely resembled those of the all-down pH 4.0 structure.

At pH 4.0, each of the RBD-switches closely resembled each other. The most dramatic refolding relative to the switches at pH 5.5 occurred in switch B, where the guanidinium of residue $Arg847_B$ swivels over 25 Å from interacting in an inter-protomer manner with $SD2_A$ to interacting in an intra-protomer manner with NTD_B of the same protomer. This swiveling breaks the coordinated displacements of domains across the protomer-protomer interface, reducing the $SD2_A$ interaction with switch by half (buried surface area of 165.1 $Å^2$).

Notably, refolding regions were observed to reside at critical inter-protomer contacts or at key joints between domains, especially the SD2 to SD1 joint, which cradles the switch of the neighboring protomer, and the $SD1_B$ joint with up-RBD_B made up of refolding residues $522\text{-}530_B$.

bioRxiv preprint doi: https://doi.org/10.1101/2020.07.04.187989; this version posted July 4, 2020. The copyright holder for this preprint (which was not certified by peer review) is the author/funder. This article is a US Government work. It is not subject to copyright under 17 USC 105 and is also made available for use under a CC0 license.

A pH-dependent switch domain locks spike in down position

The switch domain, which included aspartic acid residues at 830, 839, 843 and 848 and a disulfide linkage between Cys840 and Cys851, was located at the nexus of SD1 and SD2 from one protomer, and HR1 and NTD from the neighboring protomer. This region showed dramatic refolding. Pairwise rmsd comparisons (**Extended Data Fig. 9a**) indicated 9 of the 12 cryo-EM-determined switch structures – with at least half of their residues ordered – to segregate into two conformations: 'unprotonated-switches' and 'protonated-switches'.

Unprotonated-switches were exemplified by switches B and C at pH 5.5 and perhaps best by switch B in the pH 5.5 single-RBD up structure (**Fig. 5a, left, Supplementary Video 5**). Continuing from fusion peptide (FP_B), the N terminus of switch B formed several helical turns (833-842), extending laterally from $HR1_B$ to $SD2_A$. A turn (843-848) provided extensive contacts with $SD2_A$, before returning in helical turns (849-855) back to $HR1_B$. Unprotonated-switches were stabilized by a hydrophobic core comprising the disulfide and residues Phe833, Tyr837, Ala846, Leu849, and Phe855 (**Extended Data Fig. 9b**). Notably, all four of the unprotonated-switch aspartic acids faced solvent and appeared to be negatively charged.

Protonated-switches were exemplified by switch A at pH 5.5 and by all switches at pH 4.0 including switch B in the pH 4.0 structure (**Fig. 5a, left, Supplementary Video 5**). These switches reoriented their N-terminal helical turns to point towards SD1, swiveling the Cα-position of Arg847 over 15 Å to interact with NTD (**Extended Data Fig. 9b**) before finishing the rest of the domain with a few helical turns (848-855). Protonated switches were stabilized by a hydrophobic core comprising Tyr837 and aliphatic portions of side chain from Gln836 and Lys854 on one side of the disulfide and Ala846 and Phe855 on the other. Notably, two of the switch domain Asp residues that

bioRxiv preprint doi: https://doi.org/10.1101/2020.07.04.187989; this version posted July 4, 2020. The copyright holder for this preprint (which was not certified by peer review) is the author/funder. This article is a US Government work. It is not subject to copyright under 17 USC 105 and is also made available for use under a CC0 license.

appeared most likely to be protonated based on hydrogen bonding patterns in the pH 4.0 structure (D830 and D843) also had higher calculated pKas compared to the unprotonated switch conformation, consistent with their observed hydrogen bonds and their apparent protonation at pH 5.5 (**Extended Data Fig. 10**). Additionally, three Asp residues from the neighboring protomer (D574, D586, and D614) had higher pKas in protonated-switch conformations than in unprotonated-switch conformations. In general, our pKa calculations and structural analyses both indicated increased Asp residue protonation in the protonated-switch conformation, and reflected the expected trend of increasing numbers of protonated Asp or Glu residues at lower pH (**Extended Data Fig. 10c**).

Analysis of switch domain conformations and RBD positions (**Fig. 5b**) indicated a concordance between switches interacting with NTD (breaking coordinated interprotomer interactions) and the locking of RBDs in the down position. Thus, at pH 5.5, the unprotonated-switches in protomers B and C interacted with the SD2 domain of the neighboring protomer to transmit lateral displacements of domains. At pH 4.0, the protonated-switches interrupt this interprotomer interaction, resulting in the locking of RBDs in the down position.

Impact of Asp614Gly mutation

Analysis of SARS-CoV-2 variant sequences identifies an Asp614Gly mutation to be associated with more transmissible viral variants[7,21-24]. Our structures revealed Asp614 to be located at the key interprotomer juncture between SD2 domain and switch, forming a hydrogen bond with Tyr837 of unprotonated-switches (**Fig 5a, left**) and recognizing a backbone carbonyl in protonated-switches (**Fig. 5a, right**). To test the impact of this mutation on unfolding enthalpy, we performed DSC measurements at pH 7.4, 5.5, and 4.0 (**Fig. 5c**). While the enthalpies at pH 5.5 and 4.0 were

bioRxiv preprint doi: https://doi.org/10.1101/2020.07.04.187989; this version posted July 4, 2020. The copyright holder for this preprint (which was not certified by peer review) is the author/funder. This article is a US Government work. It is not subject to copyright under 17 USC 105 and is also made available for use under a CC0 license.

similar to those of wild-type spike, the unfolding enthalpy at pH 7.4 was dramatically increased, with the appearance of a high melting temperature peak for the variant (**Fig. 5d**), seen for the wild-type only at low pH. The dramatic difference in melting enthalpy demonstrated the substantive energetic effect of altering a interprotomer-switch interface. To test the influence of this increased unfolding enthalpy on ACE2 interaction, we performed biolayer interferometry (BLI) on dimeric ACE2 recognizing spike or the Asp614Gly variant. At pH 7.4 we observed higher binding of the wild-type spike than the Asp614Gly variant to dimeric ACE2 (**Fig. 5e, left**), consistent with DSC showing more unfolding enthalpy for the variant spike, thereby reducing its ability to bind dimeric ACE2 with avidity.

We next tried to understand the impact of the Asp614Gly mutation on the switch-based mechanism locking RBD in the down position at low pH. As switches with disorder in the region contacting SD2 were associated with "up" RBDs, we hypothesized that mutation of Asp614 to Gly would more closely mimic the loss of interaction between SD2 and switch, as exemplified by RBD_B and switch C. Indeed, BLI measurements at pH 4.0 showed dimeric ACE2 to bind the Asp614Gly variant with greater apparent affinity (**Fig. 5e, right**), consistent with the higher probability of RBDs adopting the "up" position, and providing an explanation for its increased infectivity[25]. To test the impact on antibody binding, we used BLI to measure the affinity of CR3022 to spike and Asp614Gly variant. Similar to what we observed with dimeric ACE2, CR3022 bound wild-type spike more tightly than Gly variant at physiological pH, with this behavior inverting at low pH where folding and pH switch induced antibody shedding from wild-type but less so from variant spike (**Fig. 5f**). Lastly, we tested the ability of antibody CR3022 to neutralize the Asp614Gly variant, using a pseudovirus format. The Asp614Gly variant showed a modest increase in neutralization sensitivity to CR3022 (**Fig. 5g**), indicating its conformational

bioRxiv preprint doi: https://doi.org/10.1101/2020.07.04.187989; this version posted July 4, 2020. The copyright holder for this preprint (which was not certified by peer review) is the author/funder. This article is a US Government work. It is not subject to copyright under 17 USC 105 and is also made available for use under a CC0 license.

masking to be mostly intact, with the observed increase in spike binding to CR3022 at low pH perhaps compensated with respect to neutralization by altered spike interactions with ACE2.

Discussion

Viral spikes are prime targets for neutralizing antibody, and many have evolved immune evasion, some of which resemble aspects of the pH-dependent conformational masking described here. Receptor binding-site masking with endosomal cleavage, for example, occurs with the Ebola virus glycoprotein trimer[26], and conformational masking has been previously described for the HIV-1 envelope trimer[27], which is labile and elicits antibodies of little neutralization capacity. With SARS-CoV-2, the low folding enthalpy of the spike allows antibodies like CR3022 to bind bivalently with high affinity, though also of little neutralization capacity. We show here how a pH-dependent switch locks spike in an all-RBD-down conformation, and in the process sheds antibodies like CR3022, which recognize cryptic epitopes not accessible in the all-down state.

The functional purpose of the up-down positioning of RBD domains in coronaviruses has been a point of debate, since structures of RBD-up and RBD-down have been determined[28-36]. We propose SARS-CoV-2 to use mobile RBDs, coupled with spike unfolding, to evade affinity-based mechanisms of antibody maturation by allowing tight avidity-based affinity for non- or weakly neutralizing antibodies. The impact of such evasion would be a lower neutralizing response relative to the titer of spike-binding antibody. The striking difference in unfolding enthalpy between the emerging Asp614Gly variant and its more stealthy parent may allow for comparative insight.

How– in the face of spike conformational masking – to neutralize SARS-CoV-2? We envision three scenarios. First, antibodies that block ACE2 interaction, if the spike can be prevented from binding ACE2, it will not be able to start the endosomal entry pathway. Second, antibodies

bioRxiv preprint doi: https://doi.org/10.1101/2020.07.04.187989; this version posted July 4, 2020. The copyright holder for this preprint (which was not certified by peer review) is the author/funder. This article is a US Government work. It is not subject to copyright under 17 USC 105 and is also made available for use under a CC0 license.

with extremely high affinity, we show that conformational masking reduces affinity of CR3022 at pH 4.5 by 1000-fold, so that it no longer neutralizes. However, antibodies with orders of magnitude tighter affinity might still bind and neutralize, despite a 1000-fold reduction in affinity at low endosomal pH; in this context, we note that CR3022 does have 100-fold higher affinity to the SARS-CoV spike and is able to neutralize SARS-CoV virus[6]. Third, antibodies that bind to the all-RBD down state could neutralize by locking the spike in the all-RBD down conformation. Perhaps relevant to this, many recently identified potent neutralizing antibodies appear to recognize the all-RBD down conformation[37-39]. We propose the all-down pH 4-locked conformation of the spike as a vaccine target, along the lines of what has been done to surmount evasion for other viral type 1 fusion machines, such as from RSV[40,41], HIV[42-44], and others[45-47] including SARS-CoV-2[48-50], which use alterations in conformation to elude the humoral immune response.

Acknowledgements

We thank S. Goff for discussions on viral variants and entry mechanism, R. Grassucci, Y.-C. Chi and Z. Zhang from the Cryo-EM Center at Columbia University for assistance with cryo-EM data collection, M.G. Joyce for antibody CR3022, J.S. McLellan for spike expression vector, E.H. Zhou for assistance with movies, and members of the Virology Laboratory and Vector Core, Vaccine Research Center, for discussions and comments on the manuscript. Support for this work was provided by the Intramural Research Program of the Vaccine Research Center, National Institute of Allergy and Infectious Diseases (NIAID), Federal funds from the Frederick National Laboratory for Cancer Research under Contract HHSN261200800001E (A.S., T.S., Y.T.). Cryo-EM data for the spike-ACE2 complexes were collected at the Columbia University Cryo-EM Center at the Zuckerman Institute, and at the Simons Electron Microscopy Center (SEMC) and National Center

bioRxiv preprint doi: https://doi.org/10.1101/2020.07.04.187989; this version posted July 4, 2020. The copyright holder for this preprint (which was not certified by peer review) is the author/funder. This article is a US Government work. It is not subject to copyright under 17 USC 105 and is also made available for use under a CC0 license.

for Cryo-EM Access and Training (NCCAT) located at the New York Structural Biology Center, supported by grants from the Simons Foundation (SF349247), NYSTAR, and the NIH National Institute of General Medical Sciences (GM103310). Cryo-EM datasets for individual spike proteins were collected at the National CryoEM Facility (NCEF) of the National Cancer Institute. This research was, in part, supported by the National Cancer Institute's National Cryo-EM Facility at the Frederick National Laboratory for Cancer Research under contract HSSN261200800001E. We are especially grateful to U. Baxa, A. Wier, M. Hutchison, and T. Edwards of NCEF for collecting cryo-EM data and for technical assistance with cryo-EM data processing. Frederick Research Computing Environment (FRCE) high-performance computing cluster was used for processing cryo-EM datasets of individual spike proteins.

Author Contributions

Y.T. and T.Z. determined ligand-free spike structures at pH 5.5 and 4.0; A.S.O. produced spike and Asp614Gly variant and performed DSC; J.G. M.A.R. and G.C. determined spike-ACE2 structures; P.S.K. performed SPR; A.N. carried out BLI; A.S. performed ITC; P.W. preformed neutralization assessments; J.B., W.S., I.T.T., B.Z. provided reagents; J.C.B. analyzed switch mechanics; G.-Y.C. carried out informatics analyses; J.M.S. calculated pKa; T.S. prepared ligand-free cryo-EM specimens; M.S. produced spike expression vectors; J.S. assisted with entry mechanism; S.W. assisted with manuscript preparation; R.A.F. supervised pKa calculations; D.D.H. supervised neutralization; J.R.M. supervised reagents and analyses, L.S. supervised SPR and cryo-EM studies with ACE2; P.D.K. oversaw the project and –with T.Z., Y.T., A.S.O., J.G., P.S.K. A.N., A.S., P.W., W.S., B.Z., G.-Y.C., J.M.S., S.W., and L.S. – wrote the manuscript, with all authors providing revisions and comments.

bioRxiv preprint doi: https://doi.org/10.1101/2020.07.04.187989; this version posted July 4, 2020. The copyright holder for this preprint (which was not certified by peer review) is the author/funder. This article is a US Government work. It is not subject to copyright under 17 USC 105 and is also made available for use under a CC0 license.

Competing interest declaration

The authors declare no competing interest.

Additional Information:

Supplementary Information is available for this paper.

Correspondence and requests for materials should be addressed to pdkwong@nih.gov (P.D.K.) and lss8@columbia.edu (L.S).

bioRxiv preprint doi: https://doi.org/10.1101/2020.07.04.187989; this version posted July 4, 2020. The copyright holder for this preprint (which was not certified by peer review) is the author/funder. This article is a US Government work. It is not subject to copyright under 17 USC 105 and is also made available for use under a CC0 license.

Methods

Production of spike, ACE2 receptor and antibodies

SARS-CoV-2 spike[4] and its D614G mutant were expressed by transient transfection in 293 Freestyle cells. Briefly, 1 mg of DNA was transfected into 1L of cells using Turbo293 transfection reagent, and the cells were allowed to grow at 37°C for 6 days. Following expression, the supernatant was cleared by centrifugation and filtration, and then incubated with cOmplete His-Tag Purification resin. The resin was washed with PBS containing increasing concentrations of imidazole, and the protein eluted in 20 mM Tris pH8.0, 200 mM NaCl, 300 mM Imidazole. HRV3C protease was added at a 1:20 mass ratio and incubated overnight at 4 °C to cleave the purification tags. The protein was then applied to a Superdex 200 column in PBS, after which the spike containing fractions were pooled and concentrated to 1 mg/ml. Single chain Fc tagged RBD and NTD domains were expressed in the same manner, and purified using capture by Protein A resin, followed by cleavage of the tag using HRV3C[16] and gel filtration.

Human ACE2 proteins were prepared in monomeric form (residues 1-620) and in dimeric form (residues 1-740). The expression plasmids were constructed and the protein purified as described previously[16]. Briefly, DNA sequence encoding monomeric or dimeric ACE2 was synthesized and cloned into a plasmid with an HRV3C cleavage site, monomeric Fc tag and 8xHisTag at the 3'-end. The proteins were expressed by transient transfection of 293F cells and purified from a Protein A column. The tag was removed by overnight HRV3C digestion at 4 °C. The proteins were further purified with a Superdex 200 16/60 column in 5 mM HEPES, pH7.5 and 150 mM NaCl.

For antibody preparation, DNA sequences of antibody CR3022 [6] heavy and light chains were cloned into the pVRC8400 vector, as described previously[51], expressed and purified as

bioRxiv preprint doi: https://doi.org/10.1101/2020.07.04.187989; this version posted July 4, 2020. The copyright holder for this preprint (which was not certified by peer review) is the author/funder. This article is a US Government work. It is not subject to copyright under 17 USC 105 and is also made available for use under a CC0 license.

described[16]. The Fab fragments were generated by overnight digestion with Endoproteinase LysC (New England Biolabs) at 37 °C and purified by protein A column to remove uncut IgG and Fc fragments.

Differential scanning calorimetry

DSC analyses were performed using a Microcal VP-Capillary DSC. The proteins were diluted to 0.25 mg/ml in 1X PBS or various solutions containing a final concentration of 100 mM buffer and 200mM NaCl. The buffers used were: pH 4.0-pH 5.5, Sodium Acetate; pH 6.0-pH 6.5, MES; pH 7.0, HEPES; pH 7.4, 1X PBS; pH 8.0-pH 8.5, Tris; and pH 9.0, Sodium Borate. The proteins were scanned at 1 °C per minute from 25 – 90 °C using a filter period of 25 s. Data were analyzed using the Origin based Microcal DSC Automated Analysis software, where baselines were subtracted, and peak area and T_m calculated. The melting curves and unfolding enthalpy graphs were made in Excel.

Isothermal titration calorimetry

Calorimetric titration experiments were performed at 25 °C using a VP-ITC microcalorimeter from MicroCal/Malvern Instruments (Northampton, MA, USA). The spike protein, ACE2 and Fab of CR3022 were prepared and exhaustively dialyzed against PBS, pH 7.4, prior to the experiments. Any dilution steps prior to the experiments were made using the dialysate to avoid any unnecessary heats of dilution associated with the injections. All reagents were thoroughly degassed prior to the experiments. For the direct determination of the binding to the spike protein, the solution containing either ACE2 or CR3022(Fab) was added stepwise in 10 µL aliquots to the stirred calorimetric cell (~ 1.4 ml) containing spike protein at 0.4 – 0.5 µM

bioRxiv preprint doi: https://doi.org/10.1101/2020.07.04.187989; this version posted July 4, 2020. The copyright holder for this preprint (which was not certified by peer review) is the author/funder. This article is a US Government work. It is not subject to copyright under 17 USC 105 and is also made available for use under a CC0 license.

(expressed per trimer). The concentration of titrant in the syringe was 12 – 14 μM for both ACE2 and CR3022(Fab). The effect of CR3022 on ACE2 binding to spike protein was studied by first titrating the spike protein with CR3022 until complete saturation was reached, and then performing a complete titration of the complex with ACE2. Despite the thorough dialysis, the heat of dilution/injection associated with the injection of ACE2 into the complex was considerable during the course of the titration and needed to be accounted for in the analysis. The heat evolved upon each injection was obtained from the integral of the calorimetric signal and the heat associated with binding was obtained after subtraction of the heat of dilution. The enthalpy change, ΔH, the association constant, K_a, and the stoichiometry, N, were obtained by nonlinear regression of the data to a single-site binding model using Origin with a fitting function made inhouse. Gibbs energy, ΔG, was calculated from the binding affinity using $\Delta G = -RT\ln K_a$, (R = 1.987 cal/(K × mol)) and T is the absolute temperature in kelvin). The entropy contribution to Gibbs energy, $-T\Delta S$, was calculated from the relation $\Delta G = \Delta H - T\Delta S$.

SPR binding experiments

SPR binding experiments were performed using a Biacore T200 biosensor, equipped with a Series S SA chip. The running buffer varied depending on the pH of the binding reaction; experiments at pH 7.4 were performed in a running buffer of 10 mM HEPES pH 7.4, 150 mM NaCl, 0.2 mg/ml BSA and 0.01% (v/v) Tween-20; at pH 5.5 experiments were performed in 10 mM sodium acetate pH 5.5, 150 mM NaCl, 0.2 mg/ml BSA and 0.01% (v/v) Tween-20; and at pH 4.5 in 10 mM sodium acetate pH 4.5, 150 mM NaCl, 0.2 mg/mL BSA and 0.01% (v/v) Tween-20. All measurements were performed at 25 °C.

bioRxiv preprint doi: https://doi.org/10.1101/2020.07.04.187989; this version posted July 4, 2020. The copyright holder for this preprint (which was not certified by peer review) is the author/funder. This article is a US Government work. It is not subject to copyright under 17 USC 105 and is also made available for use under a CC0 license.

Biotinylated spike and RBD were captured over independent flow cells at 700-1000 RU and 150 RU respectively for both the CR3022 IgG and the dimeric ACE2 binding experiments. To avoid the difficulty in surface regeneration that arises with slow dissociation, we used single-cycle kinetics binding experiments. CR3022 IgG was tested at analyte concentrations 36-1.33 nM prepared in running buffer at each pH, using a three-fold dilution series. In addition, CR3022 IgG was tested over the spike at higher analyte concentrations ranging 108-4 nM, 360-13.33 nM and 1000-37.04 nM at pH 4.5, only to confirm the absence of binding to the spike at pH 4.5. Dimeric ACE2 was tested at 90-3.33 nM prepared in running buffer at each pH, using a three-fold dilution series. Binding over the spike or RBD surface as well as over a streptavidin reference surface was monitored for 120 s, followed by a dissociation phase of 120-900 s depending on the interaction at 50 µl/min. Four blank buffer single cycles were performed by injecting running buffer instead of Fab to remove systematic noise from the binding signal. The data was processed and fit to 1:1 single cycle model using Scrubber 2.0 (BioLogic Software).

Cryo-EM structures of ACE2-spike complexes

SARS-CoV-2 spike was incubated with 3-fold molar excess of ACE2 receptor with a final trimer concentration of 1 mg/ml in either PBS, pH 7.4, or 10 mM sodium acetate, pH 5.5, with 150 mM NaCl. The samples (2 µl) were vitrified using a Leica EM GP and Vitrobot Mark IV plunge freezers on glow-discharged carbon-coated copper grid (protochip, CF 1.2/1.3). Data were collected on a 300 kV Titan Krios equipped with a Gatan K3-BioQuantum direct detection device using Leginon software[52]. The total dose was fractionated for 2 s over 40 raw frames. Motion correction, contrast transfer function (CTF) estimation, particle picking with topaz[53] and extraction, 2D classification, ab initio model generation, 3D refinements and local resolution

bioRxiv preprint doi: https://doi.org/10.1101/2020.07.04.187989; this version posted July 4, 2020. The copyright holder for this preprint (which was not certified by peer review) is the author/funder. This article is a US Government work. It is not subject to copyright under 17 USC 105 and is also made available for use under a CC0 license.

estimation were carried out in cryoSPARC 2.14 (ref. [54]). The 3D reconstructions were performed using C1 symmetry for all complexes as the ACE2-bound region showed flexibility that prohibited typical symmetry operations in the triple-bound complex. However, the RBD-ACE2 region was assessed in greater detail through particle expansion with C3 symmetry which was used to build that region of the model.

The coordinates of SARS CoV-2 spike ectodomain structures, PDB entries 6VXX and 6M0J[3], were employed as initial models for fitting the cryo-EM map of theACE2 bound structures. Manual and automated model building were iteratively performed using Coot[55] and real space refinement in Phenix to accurately fit the coordinates to the electron density map. Molprobity[56] was used to validate geometry and check structure quality. UCSF ChimeraX[57] was used for map-fitting cross correlation calculation (Fit-in-Map tool) and for figure preparation.

Negative-stain electron microscopy

The following buffers were used to study SARS-CoV-2 S conformation at different pH: 0.1 M sodium acetate (pH 3.6–5.5), PBS (pH 7.4), 0.1 M Trizma-HCl (pH 8.8). A sample of SARS-CoV-2 S with a concentration of 1 mg/ml was diluted with the target buffer 10 times, and the diluted sample was incubated on ice for 15 min. Immediately before negative staining, the sample was further diluted 5 times with the following buffer: 10 mM sodium acetate, 150 mM NaCl (for pH 3.6–5.5); 10 mM HEPES, 150 mM NaCl (for pH 7.4); 10 mM Trizma-HCl, 150 mM NaCl (for pH 8.8). A 4.7-µl drop of the diluted sample was applied to a glow-discharged carbon-coated copper grid for 10-15 s. The drop was removed with filter paper, and the grid was washed by applying consecutively three 4.7-µl drops of the buffer used for diluting the sample and removing them with filter paper. Protein molecules adsorbed to the carbon were negatively stained by

bioRxiv preprint doi: https://doi.org/10.1101/2020.07.04.187989; this version posted July 4, 2020. The copyright holder for this preprint (which was not certified by peer review) is the author/funder. This article is a US Government work. It is not subject to copyright under 17 USC 105 and is also made available for use under a CC0 license.

applying consecutively three 4.7-µl drops of 0.75% uranyl formate in the same manner. The grid was air-dried and screened for staining quality and particle density using a Hitachi H-7650 transmission electron microscope (TEM). Datasets were collected using an FEI T20 TEM equipped with an Eagle CCD camera. The microscope was operated at 200 kV, the pixel size was 2.2 Å (nominal magnification: 100,000), and the defocus was -1.2 µm. SerialEM[58] was used for data collection. Particles were picked automatically and extracted into 160x160- or 192x192-pixel boxes using in-house written software (YT, unpublished). 2D classification was performed using Relion 1.4 and Relion 3.0 [59].

Cryo-EM specimen preparation and data collection of individual spikes

A sample of SARS-CoV-2 S in PBS with a protein concentration of 1 mg/ml was diluted to 0.5 mg/ml using 0.2 M sodium acetate, pH 4.0 or pH 5.5 (final sodium acetate concentration: 0.1 M). Separate measurements with a pH meter confirmed that combining equal volumes of PBS and 0.2 M sodium acetate, pH 4.0 or pH 5.5, produces solutions with pH 4.0 and pH 5.5, respectively. Quantifoil R 2/2 gold grids were used for specimen preparation. The grids were glow-discharged using a PELCO easiGlow device (air pressure: 0.39 mBar, current: 20 mA, duration: 30 s) immediately before vitrification. Cryo-EM grids were prepared by plunge-freezing in liquid ethane using an FEI Vitrobot Mark IV plunger with the following settings: chamber temperature of 4°C, chamber humidity of 95%, blotting force of -5, blotting time of 5 s, and drop volume of 2.7 µl. Datasets were collected at the National CryoEM Facility (NCEF), National Cancer Institute, on a Thermo Scientific Titan Krios G3 electron microscope equipped with a Gatan Quantum GIF energy filter (slit width: 20 eV) and a Gatan K3 direct electron detector. Four movies per hole were recorded in the counting mode using Latitude software. The dose rate was 13.4 e^-/s/pixel.

bioRxiv preprint doi: https://doi.org/10.1101/2020.07.04.187989; this version posted July 4, 2020. The copyright holder for this preprint (which was not certified by peer review) is the author/funder. This article is a US Government work. It is not subject to copyright under 17 USC 105 and is also made available for use under a CC0 license.

Cryo-EM data processing and structural refinement for individual spikes

Each dataset was divided into subsets which were initially processed independently in parallel using Frederick Research Computing Environment (FRCE) computing cluster and later combined for the final refinement. Movie frame alignment was performed using MotionCorr2 [60]. Ctffind4 was used to determine the parameters of CTF[61]. The remaining processing steps were performed using Relion 3.0 (ref. [59]) unless otherwise stated. For spike at pH 4.0, a small particle set was selected manually and used to obtain 2D classes which were utilized as templates to select a larger set of particles. An initial 3D model was obtained using EMAN 2.1[62] from the 2D classes generated from this extended particle set. This 3D model was then subjected to 3D auto-refinement, and the resulting map was used to generate low-pass filtered picking templates for the entire dataset. For spike at pH 5.5, particle picking was performed with cryOLO 1.5[63] using a general network model, and an initial 3D model was obtained with EMAN 2.1 from a subset of resulting 2D classes. The following steps included rounds of 3D classification, 3D auto-refinement, CTF refinement, and particle polishing. Map resolutions were calculated using the gold-standard approach[64] at the FSC curve threshold of 0.143. ResMap 1.1.4 was used to asses local resolution[65]. Local map sharpening was performed using phenix.auto_sharpen[66]. SPIDER 22.1 was used for map conversion and re-sizing[67]. Correlations between cryo-EM maps and atomic models were assessed using phenix.mtriage[68]. UCSF Chimera was used for docking and visualization[69]. Despite the fact that C3 symmetry was imposed during the reconstruction of spike for the pH 4.0 dataset, the resulting map displayed some asymmetrical features in some regions, such as that around residue 830. Therefore, the three chains of the atomic model were built and refined individually. The coordinates of SARS CoV-2 spike ectodomain structures, PDB entries

bioRxiv preprint doi: https://doi.org/10.1101/2020.07.04.187989; this version posted July 4, 2020. The copyright holder for this preprint (which was not certified by peer review) is the author/funder. This article is a US Government work. It is not subject to copyright under 17 USC 105 and is also made available for use under a CC0 license.

6VXX and 6VYB, were used as initial models for fitting the cryo-EM map of the spike structures at pH 4.0 and pH 5.5 structures. Iterative model building and real space refinement were carried out using Coot[55] and Phenix to accurately fit the coordinates to the electron density map. Molprobity[56] was used to validate geometry and check structure quality.

3D variability analysis of cryo-EM structures of individual spikes and analysis of conformations of the RBD

For 3D variability analysis, a subset of 100,000 particles randomly selected from the final particle set at pH 5.5 was exported into cryoSPARC 2.15 [54], and a homogeneous refinement was performed without imposing symmetry. The 3D variability analysis was set up to use three eigenvectors of the 3D covariance, and 20 frames were used for visualization of results. The eigenvectors describing movements of the RBD were identified via examining the resulting volume series and corresponding variability movies (Supplementary Videos 1-4).

The structural heterogeneity of the consensus pH 5.5 map in the RBD region was analyzed using local 3D classification. To obtain an accurate mask encompassing the conformational space of the dynamic RBD, the four 3D variability volumes corresponding to the beginning and the end of the trajectories defined by eigenvectors 0 and 2 were first aligned to the consensus cryo-EM map. For each of the four volumes, the density corresponding to the dynamic RBD was isolated by performing volume segmentation in UCSF Chimera [69]. These RBD sub-volumes were added together, and a soft mask was created from the resulting composite volume by low-pass filtering the density to 15 Å, extending the resulting volume by 2 pixels, and adding a soft edge of 5 pixels using relion_mask_create. Local 3D classification of the consensus dataset within this mask was

bioRxiv preprint doi: https://doi.org/10.1101/2020.07.04.187989; this version posted July 4, 2020. The copyright holder for this preprint (which was not certified by peer review) is the author/funder. This article is a US Government work. It is not subject to copyright under 17 USC 105 and is also made available for use under a CC0 license.

performed without particle alignment in Relion 3 [59], followed by global 3D refinement of each of the resulting six maps.

Identification of SARS-CoV-2 spike refolding regions between pH 5.5 and pH 4.0 structures.

We used a sliding window of 11 amino acids and 21 amino acids respectively to align and calculate backbone (C, Ca, O, N) rmsd values between the pH 4 structure (protomer B) and pH 5.5 single-RBD-up or pH 5.5 all-RBD-down structures, respectively, using PyMol (Version 2.3.4). Calculation was omitted if the specified residue range had less than 22 backbone atoms. The average rmsd values of pH 5.5 single-RBD-up conformation 1 and conformation 2 were reported for pH 5.5 single-RBD-up analysis. The refolding regions were defined as residues with greater than 2-Å rmsd. Refolding regions with more than one consecutive residues were further considered, and single residue gaps were ignored when determining the residue ranges. Manual inspection revealed 11 amino acid-window to correspond better with domain movements. Therefore, the results from only 11 amino acid-window analysis were reported.

Bio-layer interferometry (BLI)

A FortéBio Octet HTX instrument (FortéBio) was used to assess binding over a wide pH range. Experiments were setup in tilted black 384-well plates (Geiger Bio-One) in 10mM of the corresponding buffer, plus 150mM NaCl, 0.02% Tween20, 0.1% BSA and 0.05% sodium azide. Buffers used for pH 8.0 to 4.0 are as described above in the DSC section. Plates were agitated at 1,000 rpm, and the temperature was set to 30°C. Anti-human IgG Fc capture biosensors (FortéBio) were used to immobilize 300nM CR3022 IgG or dimeric ACE2-Fc for 150 seconds at pH 7.4. Following loading of CR3022 IgG, sensors were placed in the pH 7.4 buffer for 30 seconds and

bioRxiv preprint doi: https://doi.org/10.1101/2020.07.04.187989; this version posted July 4, 2020. The copyright holder for this preprint (which was not certified by peer review) is the author/funder. This article is a US Government work. It is not subject to copyright under 17 USC 105 and is also made available for use under a CC0 license.

then equilibrated in the respective pH buffer for 180 seconds. Binding was measured for 180 seconds in 200 nM spike or D614G mutant. Binding quantification (Fig. 5d, e) was performed using the response value (nm) in the last second of the association step. Dissociation in the respective buffer was recorded for 300 seconds.

pKa calculations

Individual residue pKas were calculated for the pH 4.0 all-down, pH 5.5 all-down, and pH 5.5 single-up (conformations 1 and 2) structures using PROPKA[70,71]. For residues in the chain B 830-855 switch domains and titratable residues within 5Å of the switch domain, pKa data were analyzed and plotted using R (https://www.R-project.org/) in RStudio (http://www.rstudio.com/) with the ggplot2 library[72] and structural figures were made using PyMOL.

Pseudovirus construction and neutralization assessment

Recombinant Indiana vesiculovirus (rVSV) expressing SARS-CoV-2 spike was generated as previously described[73,74]. HEK293T cells were grown to 80% confluency before transfection with pCMV3-SARS-CoV-2-spike (kindly provided by Peihui Wang, Shandong University, China) or the D614G variant (constructed by site-directed mutagenesis) using FuGENE 6 (Promega). The next day, medium was removed and VSV-G pseudotyped ΔG-luciferase (G*ΔG-luciferase, Kerafast) was used to infect the cells in DMEM at an MOI of 3 for 1 h before washing the cells with 1X DPBS three times. DMEM supplemented with 2% fetal bovine serum and 100 I.U./mL of penicillin and 100 μg/mL of streptomycin was added to the inoculated cells. The supernatant was harvested the following day and clarified by centrifugation at 3000 rpm for 10 min before aliquoting and storing at −80°C.

bioRxiv preprint doi: https://doi.org/10.1101/2020.07.04.187989; this version posted July 4, 2020. The copyright holder for this preprint (which was not certified by peer review) is the author/funder. This article is a US Government work. It is not subject to copyright under 17 USC 105 and is also made available for use under a CC0 license.

Neutralization assays were performed by incubating pseudoviruses with serial dilutions of antibodies and scored by the reduction in luciferase gene expression. In brief, Vero E6 cells (ATCC) were seeded in a 96-well plate at a concentration of 2×10^4 cells per well. Pseudoviruses were incubated the next day with serial dilutions of the antibodies in triplicate for 30 min at 37°C. The mixture was added to cultured cells and incubated for an additional 24 h. The luminescence was measured by Britelite plus Reporter Gene Assay System (PerkinElmer). IC_{50} was defined as the dilution at which the relative light units (RLUs) were reduced by 50% compared with the virus control wells (virus + cells) after subtraction of the background RLUs in the control groups with cells only. The IC_{50} values were calculated using non-linear regression in GraphPad Prism 8.

bioRxiv preprint doi: https://doi.org/10.1101/2020.07.04.187989; this version posted July 4, 2020. The copyright holder for this preprint (which was not certified by peer review) is the author/funder. This article is a US Government work. It is not subject to copyright under 17 USC 105 and is also made available for use under a CC0 license.

References

1 Callaway, E., Cyranoski, D., Mallapaty, S., Stoye, E. & Tollefson, J. The coronavirus pandemic in five powerful charts. *Nature* **579**, 482-483, doi:10.1038/d41586-020-00758-2 (2020).

2 Zhou, P. *et al.* A pneumonia outbreak associated with a new coronavirus of probable bat origin. *Nature* **579**, 270-273, doi:10.1038/s41586-020-2012-7 (2020).

3 Walls, A. C. *et al.* Structure, Function, and Antigenicity of the SARS-CoV-2 Spike Glycoprotein. *Cell* **181**, 281-292 e286, doi:10.1016/j.cell.2020.02.058 (2020).

4 Wrapp, D. *et al.* Cryo-EM structure of the 2019-nCoV spike in the prefusion conformation. *Science* **367**, 1260-1263, doi:10.1126/science.abb2507 (2020).

5 ter Meulen, J. *et al.* Human monoclonal antibody combination against SARS coronavirus: synergy and coverage of escape mutants. *PLoS Med* **3**, e237, doi:10.1371/journal.pmed.0030237 (2006).

6 Yuan, M. *et al.* A highly conserved cryptic epitope in the receptor binding domains of SARS-CoV-2 and SARS-CoV. *Science* **368**, 630-633, doi:10.1126/science.abb7269 (2020).

7 Korber, B. *et al.* Spike mutation pipeline reveals the emergence of a more transmissible form of SARS-CoV-2. *bioRxiv*, 2020.2004.2029.069054, doi:10.1101/2020.04.29.069054 (2020).

8 Hoffmann, M. *et al.* SARS-CoV-2 Cell Entry Depends on ACE2 and TMPRSS2 and Is Blocked by a Clinically Proven Protease Inhibitor. *Cell* **181**, 271-280 e278, doi:10.1016/j.cell.2020.02.052 (2020).

9 Watanabe, Y., Allen, J. D., Wrapp, D., McLellan, J. S. & Crispin, M. Site-specific glycan analysis of the SARS-CoV-2 spike. *Science*, doi:10.1126/science.abb9983 (2020).

10 Zhou, D., Tian, X., Qi, R., Peng, C. & Zhang, W. Identification of 22 N-glycosites on spike glycoprotein of SARS-CoV-2 and accessible surface glycopeptide motifs: implications for vaccination and antibody therapeutics. *Glycobiology*, doi:10.1093/glycob/cwaa052 (2020).

11 Robbiani, D. F. *et al.* Convergent antibody responses to SARS-CoV-2 in convalescent individuals. *Nature*, doi:10.1038/s41586-020-2456-9 (2020).

12 Alvarez-Moreno, C. A. & Rodriguez-Morales, A. J. Testing Dilemmas: Post negative, positive SARS-CoV-2 RT-PCR - is it a reinfection? *Travel Med Infect Dis*, 101743, doi:10.1016/j.tmaid.2020.101743 (2020).

13 Hoang, V. T., Dao, T. L. & Gautret, P. Recurrence of positive SARS-CoV-2 in patients recovered from COVID-19. *J Med Virol*, doi:10.1002/jmv.26056 (2020).

14 Kang, H., Wang, Y., Tong, Z. & Liu, X. Retest positive for SARS-CoV-2 RNA of "recovered" patients with COVID-19: Persistence, sampling issues, or re-infection? *J Med Virol*, doi:10.1002/jmv.26114 (2020).

15 Huo, J. *et al.* Neutralization of SARS-CoV-2 by Destruction of the Prefusion Spike. *Cell Host Microbe*, doi:10.1016/j.chom.2020.06.010 (2020).

16 Zhou, T. *et al.* Structure-Based Design with Tag-Based Purification and In-Process Biotinylation Enable Streamlined Development of SARS-CoV-2 Spike Molecular Probes. *bioRxiv*, 2020.2006.2022.166033, doi:10.1101/2020.06.22.166033 (2020).

17 Robertson, A. D. & Murphy, K. P. Protein Structure and the Energetics of Protein Stability. *Chem Rev* **97**, 1251-1268, doi:10.1021/cr960383c (1997).

18 Lan, J. *et al.* Structure of the SARS-CoV-2 spike receptor-binding domain bound to the ACE2 receptor. *Nature* **581**, 215-220, doi:10.1038/s41586-020-2180-5 (2020).

bioRxiv preprint doi: https://doi.org/10.1101/2020.07.04.187989; this version posted July 4, 2020. The copyright holder for this preprint (which was not certified by peer review) is the author/funder. This article is a US Government work. It is not subject to copyright under 17 USC 105 and is also made available for use under a CC0 license.

19 Shang, J. *et al.* Structural basis of receptor recognition by SARS-CoV-2. *Nature* **581**, 221-224, doi:10.1038/s41586-020-2179-y (2020).

20 Wang, Q. *et al.* Structural and Functional Basis of SARS-CoV-2 Entry by Using Human ACE2. *Cell* **181**, 894-904 e899, doi:10.1016/j.cell.2020.03.045 (2020).

21 Daniloski, Z., Guo, X. & Sanjana, N. E. The D614G mutation in SARS-CoV-2 Spike increases transduction of multiple human cell types. *bioRxiv*, 2020.2006.2014.151357, doi:10.1101/2020.06.14.151357 (2020).

22 Hu, J. *et al.* The D614G mutation of SARS-CoV-2 spike protein enhances viral infectivity and decreases neutralization sensitivity to individual convalescent sera. *bioRxiv*, 2020.2006.2020.161323, doi:10.1101/2020.06.20.161323 (2020).

23 Ozono, S. *et al.* Naturally mutated spike proteins of SARS-CoV-2 variants show differential levels of cell entry. *bioRxiv*, 2020.2006.2015.151779, doi:10.1101/2020.06.15.151779 (2020).

24 Ke, Z. *et al.* Structures, conformations and distributions of SARS-CoV-2 spike protein trimers on intact virions. *bioRxiv*, 2020.2006.2027.174979, doi:10.1101/2020.06.27.174979 (2020).

25 Zhang, L. *et al.* The D614G mutation in the SARS-CoV-2 spike protein reduces S1 shedding and increases infectivity. *bioRxiv*, 2020.2006.2012.148726, doi:10.1101/2020.06.12.148726 (2020).

26 Kaletsky, R. L., Simmons, G. & Bates, P. Proteolysis of the Ebola virus glycoproteins enhances virus binding and infectivity. *J Virol* **81**, 13378-13384, doi:10.1128/JVI.01170-07 (2007).

27 Kwong, P. D. *et al.* HIV-1 evades antibody-mediated neutralization through conformational masking of receptor-binding sites. *Nature* **420**, 678-682 (2002).

28 Beniac, D. R., Andonov, A., Grudeski, E. & Booth, T. F. Architecture of the SARS coronavirus prefusion spike. *Nat Struct Mol Biol* **13**, 751-752, doi:10.1038/nsmb1123 (2006).

29 Gui, M. *et al.* Cryo-electron microscopy structures of the SARS-CoV spike glycoprotein reveal a prerequisite conformational state for receptor binding. *Cell Res* **27**, 119-129, doi:10.1038/cr.2016.152 (2017).

30 Kirchdoerfer, R. N. *et al.* Pre-fusion structure of a human coronavirus spike protein. *Nature* **531**, 118-121, doi:10.1038/nature17200 (2016).

31 Song, W., Gui, M., Wang, X. & Xiang, Y. Cryo-EM structure of the SARS coronavirus spike glycoprotein in complex with its host cell receptor ACE2. *PLoS Pathog* **14**, e1007236, doi:10.1371/journal.ppat.1007236 (2018).

32 Walls, A. C. *et al.* Glycan shield and epitope masking of a coronavirus spike protein observed by cryo-electron microscopy. *Nat Struct Mol Biol* **23**, 899-905, doi:10.1038/nsmb.3293 (2016).

33 Yuan, Y. *et al.* Cryo-EM structures of MERS-CoV and SARS-CoV spike glycoproteins reveal the dynamic receptor binding domains. *Nat Commun* **8**, 15092, doi:10.1038/ncomms15092 (2017).

34 Pallesen, J. *et al.* Immunogenicity and structures of a rationally designed prefusion MERS-CoV spike antigen. *Proceedings of the National Academy of Sciences* **114**, E7348-E7357, doi:10.1073/pnas.1707304114 (2017).

bioRxiv preprint doi: https://doi.org/10.1101/2020.07.04.187989; this version posted July 4, 2020. The copyright holder for this preprint (which was not certified by peer review) is the author/funder. This article is a US Government work. It is not subject to copyright under 17 USC 105 and is also made available for use under a CC0 license.

35 Shang, J. *et al.* Cryo-EM structure of infectious bronchitis coronavirus spike protein reveals structural and functional evolution of coronavirus spike proteins. *PLoS Pathog* **14**, e1007009, doi:10.1371/journal.ppat.1007009 (2018).

36 Shang, J. *et al.* Structure of mouse coronavirus spike protein complexed with receptor reveals mechanism for viral entry. *PLoS Pathog* **16**, e1008392, doi:10.1371/journal.ppat.1008392 (2020).

37 Liu, L. *et al.* Potent Neutralizing Monoclonal Antibodies Directed to Multiple Epitopes on the SARS-CoV-2 Spike. *bioRxiv*, 2020.2006.2017.153486, doi:10.1101/2020.06.17.153486 (2020).

38 Pinto, D. *et al.* Structural and functional analysis of a potent sarbecovirus neutralizing antibody. *bioRxiv*, doi:10.1101/2020.04.07.023903 (2020).

39 Pinto, D. *et al.* Cross-neutralization of SARS-CoV-2 by a human monoclonal SARS-CoV antibody. *Nature*, doi:10.1038/s41586-020-2349-y (2020).

40 Joyce, M. G. *et al.* Iterative structure-based improvement of a fusion-glycoprotein vaccine against RSV. *Nat Struct Mol Biol* **23**, 811-820, doi:10.1038/nsmb.3267 (2016).

41 Krarup, A. *et al.* A highly stable prefusion RSV F vaccine derived from structural analysis of the fusion mechanism. *Nat Commun* **6**, 8143, doi:10.1038/ncomms9143 (2015).

42 Kwon, Y. D. *et al.* Crystal structure, conformational fixation and entry-related interactions of mature ligand-free HIV-1 Env. *Nat Struct Mol Biol* **22**, 522-531, doi:10.1038/nsmb.3051 (2015).

43 de Taeye, S. W. *et al.* Immunogenicity of Stabilized HIV-1 Envelope Trimers with Reduced Exposure of Non-neutralizing Epitopes. *Cell* **163**, 1702-1715, doi:10.1016/j.cell.2015.11.056 (2015).

44 Dey, B. *et al.* Structure-based stabilization of HIV-1 gp120 enhances humoral immune responses to the induced co-receptor binding site. *PLoS Pathog* **5**, e1000445, doi:10.1371/journal.ppat.1000445 (2009).

45 Rutten, L. *et al.* Structure-Based Design of Prefusion-Stabilized Filovirus Glycoprotein Trimers. *Cell Rep* **30**, 4540-4550 e4543, doi:10.1016/j.celrep.2020.03.025 (2020).

46 Stewart-Jones, G. B. E. *et al.* Structure-based design of a quadrivalent fusion glycoprotein vaccine for human parainfluenza virus types 1-4. *Proc Natl Acad Sci U S A* **115**, 12265-12270, doi:10.1073/pnas.1811980115 (2018).

47 Slon-Campos, J. L. *et al.* A protective Zika virus E-dimer-based subunit vaccine engineered to abrogate antibody-dependent enhancement of dengue infection. *Nat Immunol* **20**, 1291-1298, doi:10.1038/s41590-019-0477-z (2019).

48 Henderson, R. *et al.* Controlling the SARS-CoV-2 Spike Glycoprotein Conformation. *bioRxiv*, doi:10.1101/2020.05.18.102087 (2020).

49 Hsieh, C.-L. *et al.* Structure-based Design of Prefusion-stabilized SARS-CoV-2 Spikes. *bioRxiv*, 2020.2005.2030.125484, doi:10.1101/2020.05.30.125484 (2020).

50 Xiong, X. *et al.* A thermostable, closed, SARS-CoV-2 spike protein trimer. *bioRxiv*, 2020.2006.2015.152835, doi:10.1101/2020.06.15.152835 (2020).

51 Wu, X. *et al.* Focused evolution of HIV-1 neutralizing antibodies revealed by structures and deep sequencing. *Science* **333**, 1593-1602, doi:10.1126/science.1207532 (2011).

52 Suloway, C. *et al.* Automated molecular microscopy: the new Leginon system. *J Struct Biol* **151**, 41-60, doi:10.1016/j.jsb.2005.03.010 (2005).

bioRxiv preprint doi: https://doi.org/10.1101/2020.07.04.187989; this version posted July 4, 2020. The copyright holder for this preprint (which was not certified by peer review) is the author/funder. This article is a US Government work. It is not subject to copyright under 17 USC 105 and is also made available for use under a CC0 license.

53 Bepler, T. *et al.* Positive-unlabeled convolutional neural networks for particle picking in cryo-electron micrographs. *Nat Methods* **16**, 1153-1160, doi:10.1038/s41592-019-0575-8 (2019).

54 Punjani, A., Rubinstein, J. L., Fleet, D. J. & Brubaker, M. A. cryoSPARC: algorithms for rapid unsupervised cryo-EM structure determination. *Nat Methods* **14**, 290-296, doi:10.1038/nmeth.4169 (2017).

55 Emsley, P. & Cowtan, K. Coot: model-building tools for molecular graphics. *Acta Crystallogr D Biol Crystallogr* **60**, 2126-2132, doi:S0907444904019158 [pii]10.1107/S0907444904019158 (2004).

56 Davis, I. W., Murray, L. W., Richardson, J. S. & Richardson, D. C. MOLPROBITY: structure validation and all-atom contact analysis for nucleic acids and their complexes. *Nucleic Acids Res* **32**, W615-619, doi:10.1093/nar/gkh39832/suppl_2/W615 [pii] (2004).

57 Goddard, T. D. *et al.* UCSF ChimeraX: Meeting modern challenges in visualization and analysis. *Protein Sci* **27**, 14-25, doi:10.1002/pro.3235 (2018).

58 Mastronarde, D. N. Automated electron microscope tomography using robust prediction of specimen movements. *J Struct Biol* **152**, 36-51, doi:10.1016/j.jsb.2005.07.007 (2005).

59 Scheres, S. H. RELION: implementation of a Bayesian approach to cryo-EM structure determination. *J Struct Biol* **180**, 519-530, doi:10.1016/j.jsb.2012.09.006 (2012).

60 Zheng, S. Q. *et al.* MotionCor2: anisotropic correction of beam-induced motion for improved cryo-electron microscopy. *Nat Methods* **14**, 331-332, doi:10.1038/nmeth.4193 (2017).

61 Rohou, A. & Grigorieff, N. CTFFIND4: Fast and accurate defocus estimation from electron micrographs. *J Struct Biol* **192**, 216-221, doi:10.1016/j.jsb.2015.08.008 (2015).

62 Tang, G. *et al.* EMAN2: an extensible image processing suite for electron microscopy. *J Struct Biol* **157**, 38-46, doi:10.1016/j.jsb.2006.05.009 (2007).

63 Wagner, T. *et al.* SPHIRE-crYOLO is a fast and accurate fully automated particle picker for cryo-EM. *Commun Biol* **2**, 218, doi:10.1038/s42003-019-0437-z (2019).

64 Henderson, R. *et al.* Outcome of the first electron microscopy validation task force meeting. *Structure* **20**, 205-214, doi:10.1016/j.str.2011.12.014 (2012).

65 Kucukelbir, A., Sigworth, F. J. & Tagare, H. D. Quantifying the local resolution of cryo-EM density maps. *Nat Methods* **11**, 63-65, doi:10.1038/nmeth.2727 (2014).

66 Terwilliger, T. C., Sobolev, O. V., Afonine, P. V. & Adams, P. D. Automated map sharpening by maximization of detail and connectivity. *Acta Crystallogr D Struct Biol* **74**, 545-559, doi:10.1107/S2059798318004655 (2018).

67 Frank, J. *et al.* SPIDER and WEB: processing and visualization of images in 3D electron microscopy and related fields. *J Struct Biol* **116**, 190-199, doi:10.1006/jsbi.1996.0030 (1996).

68 Afonine, P. V. *et al.* New tools for the analysis and validation of cryo-EM maps and atomic models. *Acta Crystallogr D Struct Biol* **74**, 814-840, doi:10.1107/S2059798318009324 (2018).

69 Pettersen, E. F. *et al.* UCSF Chimera--a visualization system for exploratory research and analysis. *J Comput Chem* **25**, 1605-1612, doi:10.1002/jcc.20084 (2004).

70 Olsson, M. H., Sondergaard, C. R., Rostkowski, M. & Jensen, J. H. PROPKA3: Consistent Treatment of Internal and Surface Residues in Empirical pKa Predictions. *J Chem Theory Comput* **7**, 525-537, doi:10.1021/ct100578z (2011).

bioRxiv preprint doi: https://doi.org/10.1101/2020.07.04.187989; this version posted July 4, 2020. The copyright holder for this preprint (which was not certified by peer review) is the author/funder. This article is a US Government work. It is not subject to copyright under 17 USC 105 and is also made available for use under a CC0 license.

71 Sondergaard, C. R., Olsson, M. H., Rostkowski, M. & Jensen, J. H. Improved Treatment of Ligands and Coupling Effects in Empirical Calculation and Rationalization of pKa Values. *J Chem Theory Comput* **7**, 2284-2295, doi:10.1021/ct200133y (2011).

72 Wickham, H. *ggplot2: Elegant Graphics for Data Analysis.*, (Springer-Verlag, New York, 2016).

73 Nie, J. *et al.* Establishment and validation of a pseudovirus neutralization assay for SARS-CoV-2. *Emerg Microbes Infect* **9**, 680-686, doi:10.1080/22221751.2020.1743767 (2020).

74 Whitt, M. A. Generation of VSV pseudotypes using recombinant DeltaG-VSV for studies on virus entry, identification of entry inhibitors, and immune responses to vaccines. *J Virol Methods* **169**, 365-374, doi:10.1016/j.jviromet.2010.08.006 (2010).

75 Xu, C. *et al.* Conformational dynamics of SARS-CoV-2 trimeric spike glycoprotein in complex with receptor ACE2 revealed by cryo-EM. *bioRxiv*, 2020.2006.2030.177097, doi:10.1101/2020.06.30.177097 (2020).

76 Cai, Y. *et al.* Distinct conformational states of SARS-CoV-2 spike protein. *bioRxiv*, 2020.2005.2016.099317, doi:10.1101/2020.05.16.099317 (2020).

77 Yang, A. S. & Honig, B. On the pH dependence of protein stability. *J Mol Biol* **231**, 459-474, doi:10.1006/jmbi.1993.1294 (1993).

bioRxiv preprint doi: https://doi.org/10.1101/2020.07.04.187989; this version posted July 4, 2020. The copyright holder for this preprint (which was not certified by peer review) is the author/funder. This article is a US Government work. It is not subject to copyright under 17 USC 105 and is also made available for use under a CC0 license.

Supplementary Video Legends

Supplementary Video 1. A side-view movie illustrating the trajectory of the 3D covariance described by eigenvector 0 in 3D variability analysis of individual spike at pH 5.5 (see Methods for a detailed description). A ratcheting motion of one NTD domain results in increased mobility of the corresponding RBD. A corresponding top view is presented in Supplementary Video 2.

Supplementary Video 2. A top-view movie illustrating the trajectory of the 3D covariance described by eigenvector 0 in 3D variability analysis of individual spike at pH 5.5 (see Methods for a detailed description). The RBD is up and alternates between two positions. A corresponding side view is presented in Supplementary Video 1.

Supplementary Video 3. A side-view movie illustrating the trajectory of the 3D covariance described by eigenvector 2 in 3D variability analysis of individual spike at pH 5.5 (see Methods for a detailed description). A ratcheting motion of one NTD domain results in increased mobility of the corresponding RBD. A corresponding top view is presented in Supplementary Video 4.

Supplementary Video 4. A top-view movie illustrating the trajectory of the 3D covariance described by eigenvector 2 in 3D variability analysis of individual spike at pH 5.5 (see Methods for a detailed description). The RBD alternates between an up and down position. A corresponding side view is presented in Supplementary Video 3.

Supplementary Video 5. pH-dependent domain movements in the SARS-CoV-2 spike and pH-switch refolding.

bioRxiv preprint doi: https://doi.org/10.1101/2020.07.04.187989; this version posted July 4, 2020. The copyright holder for this preprint (which was not certified by peer review) is the author/funder. This article is a US Government work. It is not subject to copyright under 17 USC 105 and is also made available for use under a CC0 license.

Figure 1

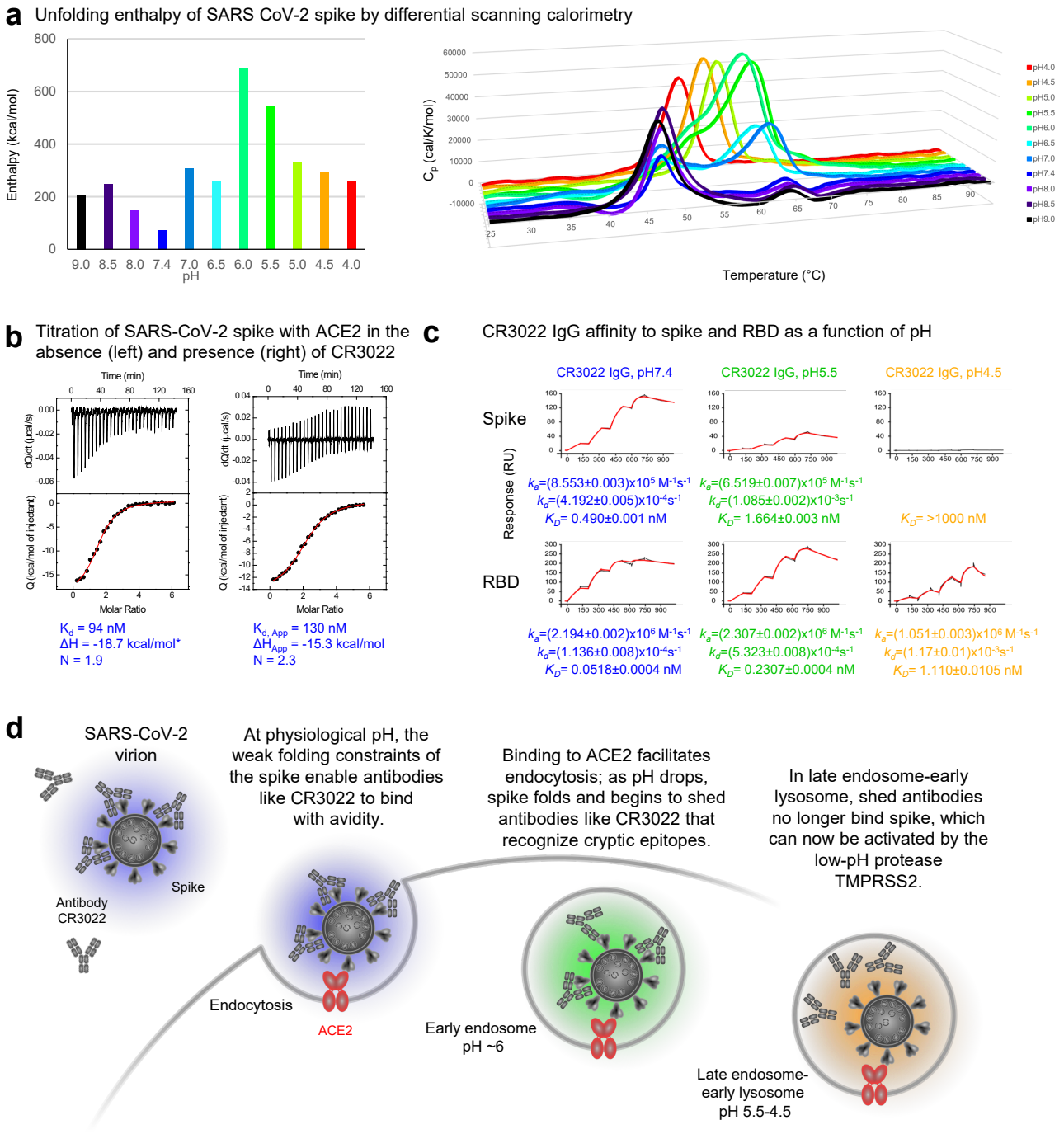

Figure 1 | SARS-CoV-2 spike is partially folded at physiological pH, where it binds ACE2 and CR3022, and more folded at lower pH, where it still binds ACE2, but not CR3022. a, Unfolding enthalpy of spike as measured by differential scanning calorimetry (DSC). Left, overall unfolding enthalpy measured as area under the curve (AUC) as a function of pH; at pH 7.4, the spike showed only ~10% the normalized unfolding enthalpy of the average globular protein. Right, unfolding enthalpy as a function of temperature. **b,** Isothermal titration calorimetry of ACE2 recognizing spike (left) or spike previously titrated with Fab CR3022 (right). **c,** Binding affinities of CR3022 to spike (top) and RBD (bottom) as a function of pH as measured by SPR. **d,** Schematic showing ACE2-dependent entry of SARS-CoV-2 and the pH-dependent shedding of antibodies like CR3022.

bioRxiv preprint doi: https://doi.org/10.1101/2020.07.04.187989; this version posted July 4, 2020. The copyright holder for this preprint (which was not certified by peer review) is the author/funder. This article is a US Government work. It is not subject to copyright under 17 USC 105 and is also made available for use under a CC0 license.

Figure 2

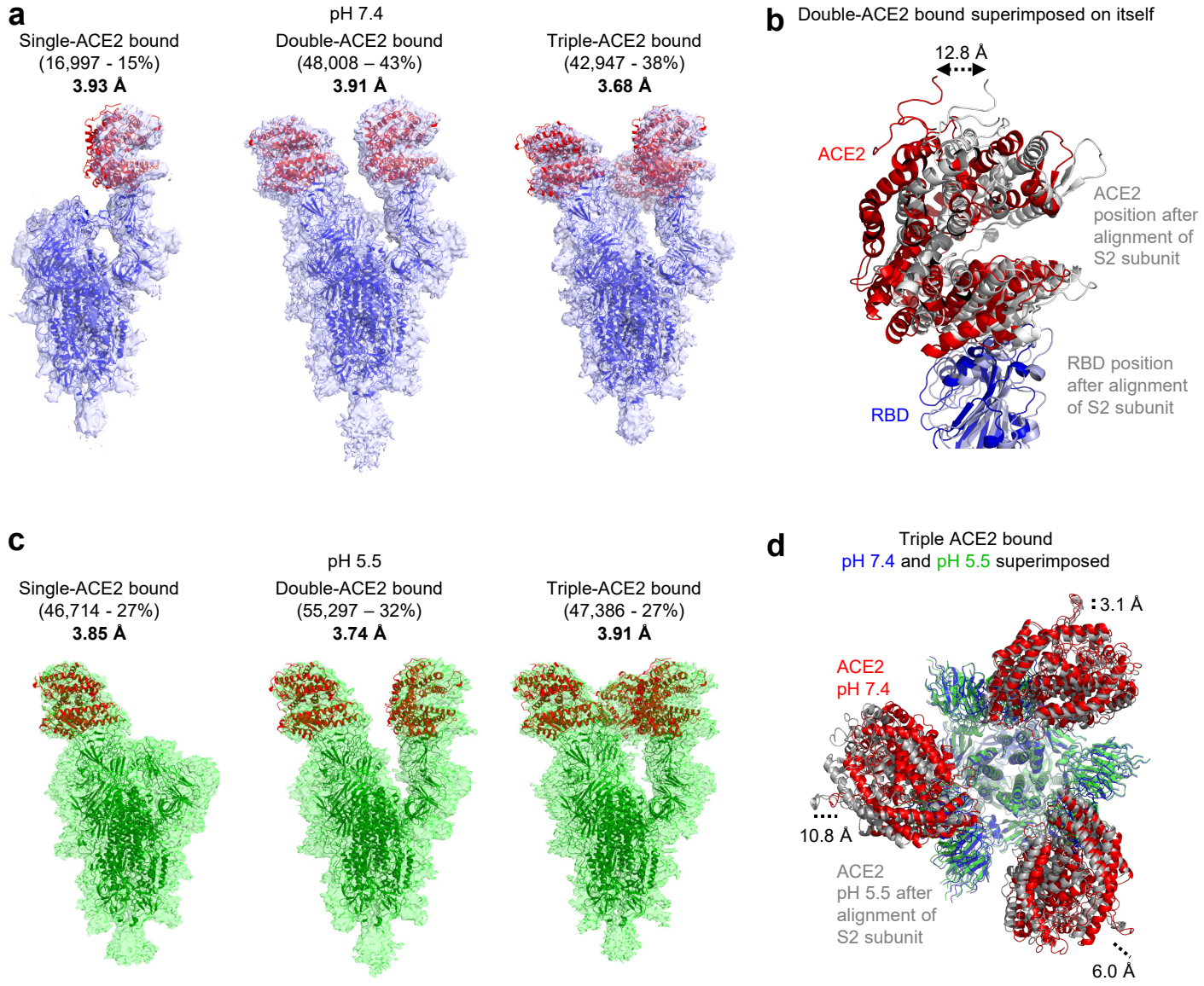

Figure 2 | Cryo-EM structures of SARS-CoV-2 spike with ACE2 show similar stoichiometries at physiological and endosomal pH. a, Cryo-EM structures of spike with single-, double-, or triple-bound ACE2 at physiological pH. **b,** Structural comparison of the two ACE2-RBD in the double ACE2-bound structure reveals different tilt angles resulting in a 12.8 Å displacement as indicated. **c**, Cryo-EM structure of spike and ACE2 at endosomal pH. **d**, Comparison of triple ACE2-bound spikes at physiological and endosomal pH. Structures were aligned by S2-subunit superposition and are displayed with the trimer perpendicular to the page and with spike colored according to pH and ACE2 colored red and gray for pH 7.4 and 5.5, respectively.

bioRxiv preprint doi: https://doi.org/10.1101/2020.07.04.187989; this version posted July 4, 2020. The copyright holder for this preprint (which was not certified by peer review) is the author/funder. This article is a US Government work. It is not subject to copyright under 17 USC 105 and is also made available for use under a CC0 license.

Figure 3

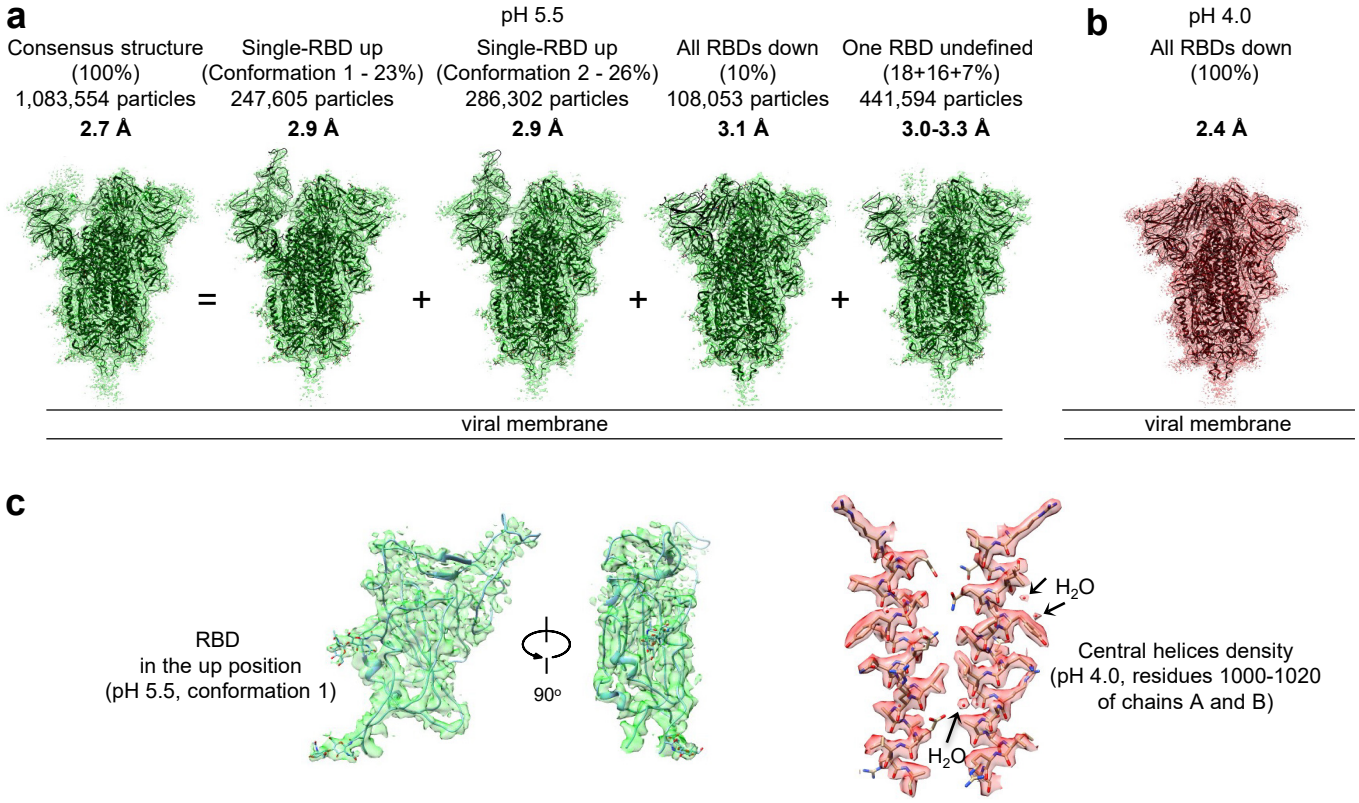

Figure 3 | Cryo-EM analyses reveal lower pH to reduce spike-conformational heterogeneity culminating in an all RBD-down conformation at pH 4.0. a, Structures at pH 5.5 with particle prevalence and resolution of determined structures. **b,** High resolution structure of spike at pH 4.0. **c**, Examples of reconstruction density. The single-up RBD in the pH 5.5 conformation 1 with density is shown to the left, and a region at the central helices of the pH 4.0 structure is shown with well-defined water molecules to the right.

bioRxiv preprint doi: https://doi.org/10.1101/2020.07.04.187989; this version posted July 4, 2020. The copyright holder for this preprint (which was not certified by peer review) is the author/funder. This article is a US Government work. It is not subject to copyright under 17 USC 105 and is also made available for use under a CC0 license.

Figure 4

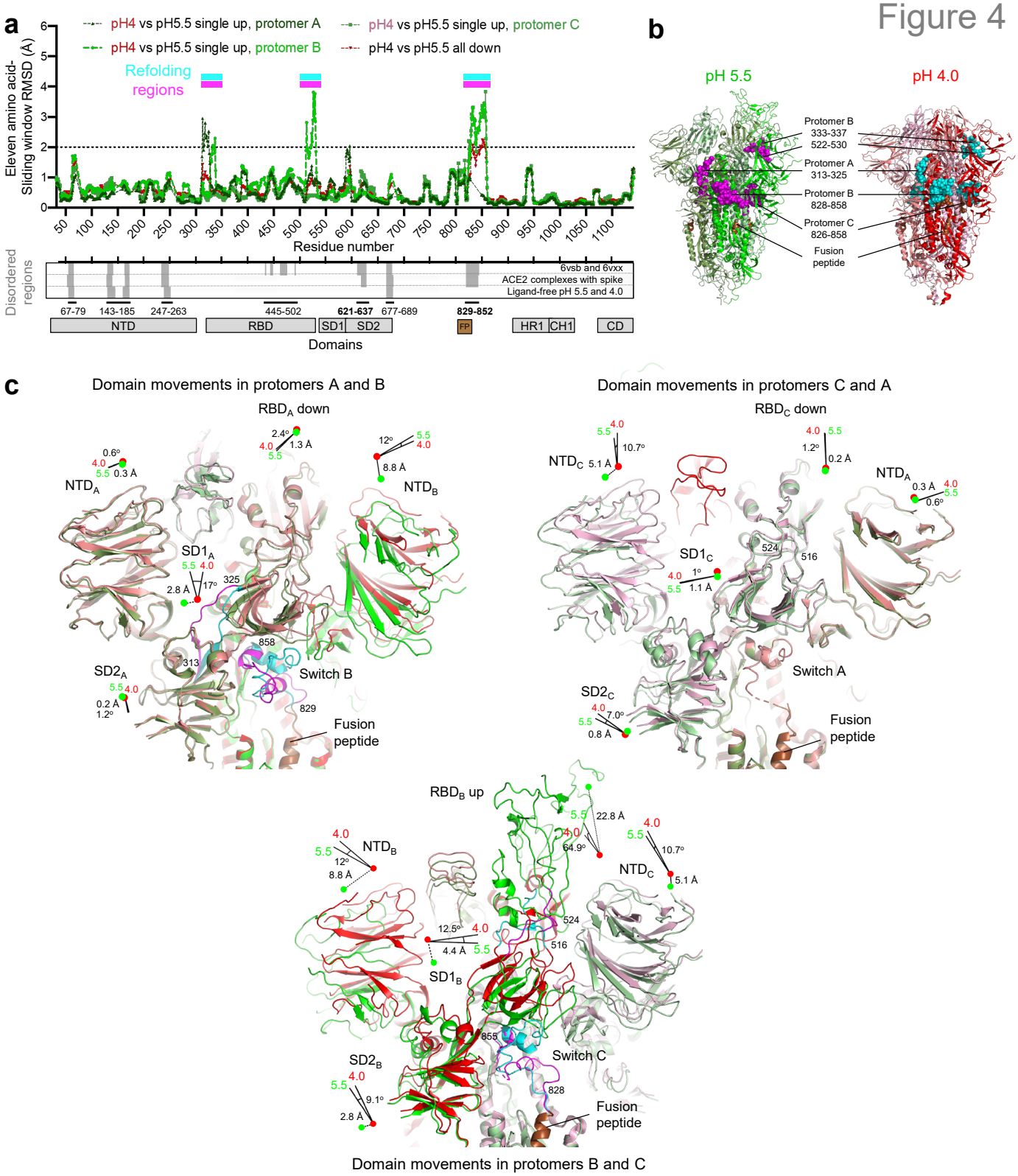

Figure 4 | A switch domain mediates RBD position. a, Identification of refolding regions through rmsd analysis with a 11-residue window (top) and comparison of disordered regions in cryo-EM structures (bottom). **b,** Refolding regions identified by sliding-window rmsd analysis are highlighted on the pH 5.5 single-up and pH 4.0 structures as spheres and are colored magenta and cyan, respectively. Protomers A, B and C of the pH 5.5 structure are each colored smudge, green or pale green, and the corresponding protomers in the pH 4.0 structure are colored salmon, red or light pink, with fusion peptide colored brown. **c,** Domain movements between pH 5.5 and 4.0. Three views are shown to depict the movements at the interfaces of protomers A/B, B/C and C/A. Extent and direction of rotation and displacement are indicated for each domain with vectors and colored dots. Refolding regions are labeled and colored as in **b**.

bioRxiv preprint doi: https://doi.org/10.1101/2020.07.04.187989; this version posted July 4, 2020. The copyright holder for this preprint (which was not certified by peer review) is the author/funder. This article is a US Government work. It is not subject to copyright under 17 USC 105 and is also made available for use under a CC0 license.

Figure 5

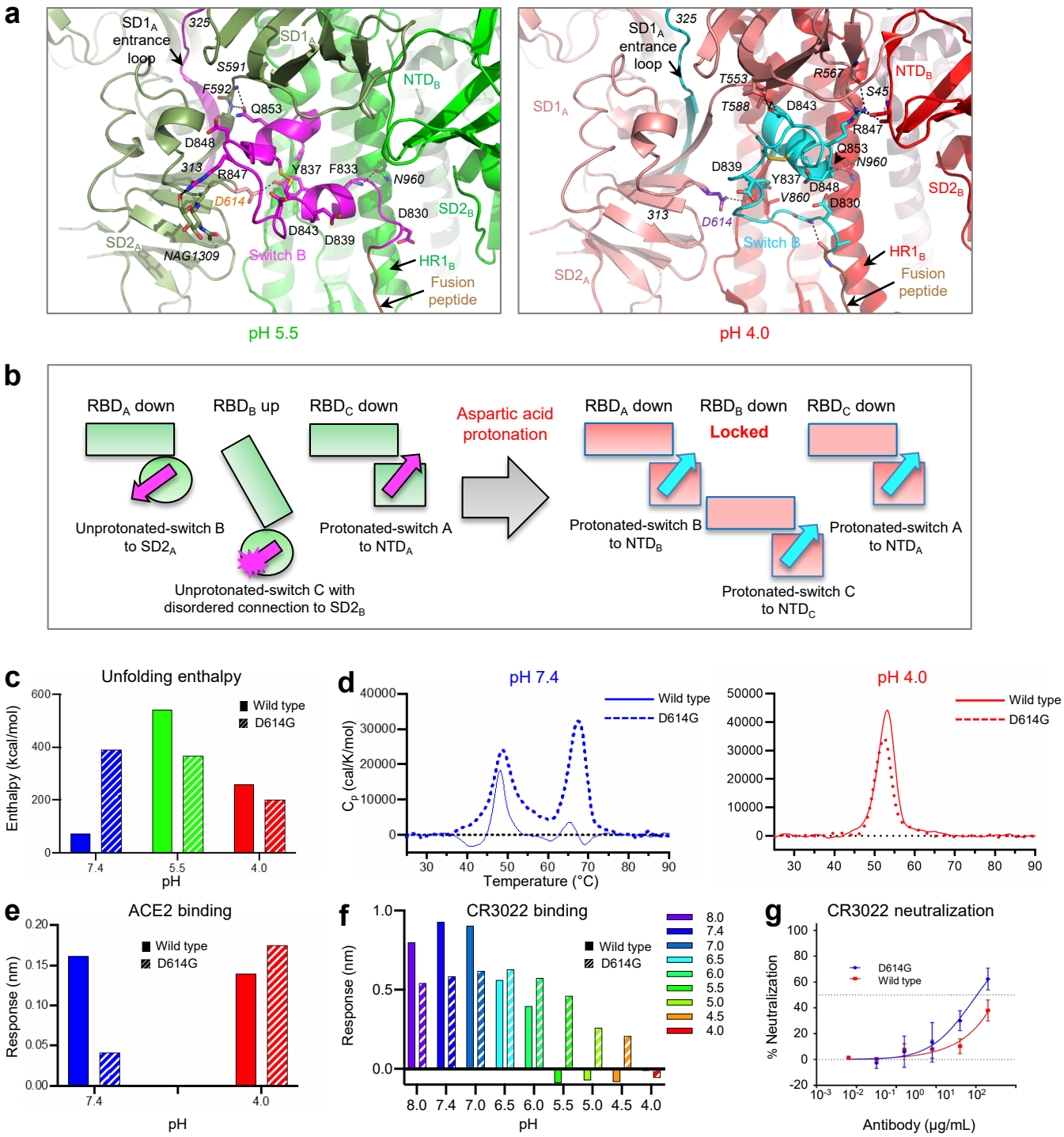

Figure 5 | Asp protonation at low pH refolds switch domain locking RBD in the down position; an Asp614Gly variant has altered interactions with ACE2 and modestly impaired conformational masking. a, Details of the pH-switch domain. Several key residues, including R847, Q853, and Y837, switched interactive partners upon refolding. Asp614 is colored orange and purple blue at pH 5.5 and pH 4.0, respectively. Surrounding residues interacting with the switch are labeled in italics, and hydrogen bonds are shown as dashed lines. **b**, Schematic of the pH-switch locking of RBD in the down position. **c**, Unfolding enthalpy measured by DSC for the spike and its Asp614Gly variant at pH 7.4, 5.5, and 4.0. **d,** Melting curves at pH 7.4 (left) and 4.0 (right). **e**, BLI measurements of ACE2 binding to the spike and its Asp614Gly variant at pH 7.4 and 4.0. **f**, BLI measurements of CR3022 binding to the spike and its D614G variant at different pHs. **g**, Pseudovirus neutralization of SARS-CoV-2 and its D614G variant by antibody CR3022.